

Antiferromagnetic semimetal terahertz photodetectors enhanced through weak localization

Received: 27 May 2024

Accepted: 10 December 2024

Published online: 02 January 2025



Dong Wang^{1,2,3,8}, Liu Yang^{2,3,8}, Zhen Hu^{1,4,8}, Fang Wang^{1,4} , Yage Yang⁴, Xiaokai Pan^{1,4}, Zhuo Dong³, Shijian Tian⁵, Libo Zhang^{1,4,6} , Li Han⁷, Mengjie Jiang^{1,5}, Keqin Tang^{2,3}, Fuxing Dai^{1,4}, Kai Zhang^{1,4} , Wei Lu^{1,4,6} , Xiaoshuang Chen^{1,4,6} , Lin Wang^{1,4}  & Weida Hu^{1,4,6} 

Effective detection is critical for terahertz applications, yet it remains hindered by the unclear mechanisms that necessitate a deeper understanding of photosensitive materials with exotic physical phenomena. Here, we investigate the terahertz detection capabilities of the two-dimensional antiferromagnetic semimetal NbFeTe₂. Our study reveals that the interaction between antiferromagnetic magnetic moments and electron spin induces disordered carriers to hop between localized states, resulting in a nonlinear increase in responsivity as temperature decreases. We integrate asymmetric electrodes to generate a sufficient Seebeck potential, enabling carriers to overcome the barrier of localized states and achieve reordering at room temperature. Additionally, the self-powered performance of the NbFeTe₂/graphene heterojunction is optimized by the built-in electric field, achieving peak responsivity of 220 V W⁻¹ and noise equivalent power of <20 pW Hz^{-1/2}. These results shed light on the potential of antiferromagnetic semimetals in large-area, high-speed imaging applications, marking a significant advancement in terahertz photonics.

Photodetectors play a pivotal role in modern communication and sensing systems that have become ubiquitous in our daily life. The raising interests in terahertz (THz) wave (loosely defined within the frequency from 0.1 THz to 10 THz) necessitates the progressive development of groundbreaking photodetection systems for a vast range of applications, such as bioassays, remote sensing, high-speed communication, and many others^{1–4}. Although commercially available

technologies exist for this particular photon-energy range, they suffer from considerable drawbacks imposed by cryogenic operation, high manufacturing costs, and difficult to integrate^{5,6}. These key priorities have prompted a major surge in interdisciplinary research within the material science and optoelectronic communities over the last decade, encompassing investigations into various physical mechanisms and a large variety of material systems that provide ad-hoc properties for the

¹State Key Laboratory for Infrared Physics, Shanghai Institute of Technical Physics, Chinese Academy of Sciences, Yutian Road 500, Shanghai 200083, China.

²School of Nano-Tech and Nano-Bionics, University of Science and Technology of China, Jinzhai Road 96, Hefei, Anhui 230026, China. ³CAS Key Laboratory of Nanophotonic Materials and Devices & Key Laboratory of Nanodevices and Applications, i-Lab, Suzhou Institute of Nano-Tech and Nano-Bionics (SINANO), Chinese Academy of Sciences, Ruoshui Road 398, Suzhou, Jiangsu 215123, China. ⁴University of Chinese Academy of Sciences, Yuquan Road 19, Beijing 100049, China. ⁵Department of Optoelectronic Science and Engineering, Donghua University, North Renmin Road 2999, Shanghai 201620, China. ⁶College of Physics and Optoelectronic Engineering, Hangzhou Institute for Advanced Study, University of Chinese Academy of Sciences, Sub-Lane Xiangshan 1, Hangzhou, Zhejiang 310024, China. ⁷College of Optical and Electronic Technology, China Jiliang University, Xueyuan Street 258, Hangzhou, Zhejiang 310018, China. ⁸These authors contributed equally: Dong Wang, Liu Yang, and Zhen Hu. ✉ e-mail: fwang@mail.sitp.ac.cn; kzhang2015@sinano.ac.cn; wanglin@mail.sitp.ac.cn

expected functionalities. As a consequence, 2D materials stand out conspicuously from conventional semiconductors in terms of fascinating optoelectronic properties, compatibility with flexible electronics, and amenable to hybridization with other materials, which have been capitalized upon for photodetection with breakthroughs in sensitivity, optical response speed, array size, dynamic range, and other indicators^{7,8}. Therefore, leveraging the unique properties of 2D materials and various light-induced effects provides an efficient strategy for device implementation. In this context, a wealth of room-temperature detection technologies have been proposed using semimetals, such as Dirac semimetal graphene, Weyl semimetals NbIrTe₄, and other gapped ones^{9–11}. These materials provide ultra-high electron mobility and high-resolution imaging capabilities in the THz band due to their linearly dispersive, topologically protected energy band in the vicinity of the Dirac point.

On the other hand, a variety of antiferromagnetic functional devices, composed of ferromagnetic-antiferromagnetic heterojunction^{12,13}, heavy-metal-oxide or Mn-based insulating bulk crystals^{14–16}, allow for the coherent manipulation of ultrafast spin exchange-dynamics. Compared to ferromagnetic counterparts, these devices excel as field-free THz emitters and in harnessing spin-to-charge current conversion through inverse spin Hall effect¹⁷. This spin-charge interconversion makes antiferromagnets an appealing choice for the generation, detection, and modulation of coherent THz signals^{18–20}. Although a few reports suggest that antiferromagnetic systems can serve as auxiliary pinning layers in spintronic devices or for magnetic information storage, whose use as photosensitive material directly manipulated by low-energy THz photons remains elusive²¹.

Intercalation doping of Fe elements in NbTe₂ (Fig. 1a) produces intra-layer ferromagnetism and inter-layer antiferromagnetism (A-type) antiferromagnetism (Fig. 1b) for NbFeTe₂ (NFT) with negligible bandgap²². The particular magnetic moments and electron spin interactions in NFT (Fig. 1c–f) result in the Anderson localization, which bind the free transport of carriers between the lattices. Meanwhile, the hopping mechanism provides a versatile platform for carriers to overcoming the potential barrier of localized states within the atomically thin semimetal layer through thermal or quantum activation²³. It is noteworthy that, unlike localized states artificially introduced through defects or photolithography, the intrinsic localization in NFTs

—arising from the interaction between antiferromagnetic magnetic moments and electron spin—offers a more direct approach for studying the behavior of nonequilibrium carriers hopping between localized states via THz detection²⁴.

In this study, we describe a THz detector strategy tailored for diverse application scenarios, leveraging the hopping mechanism observed in NFT single crystals synthesized via a chemical vapor transport (CVT) method. Our investigation combines theoretical calculations with angle resolved photoemission spectroscopy (ARPES) results to uncover the presence of carrier localization in NFT, which is attributed to the interaction between antiferromagnetic magnetic moments and spin. We develop a physical model to describe this localization, with the resulting carrier hopping behavior in the 77–200 K range, as fitted from the σ -T curve, governing the distinctive non-linear increase in responsivity with decreasing temperature. Moreover, by mitigating the confinement of localized states on carriers through the Seebeck potential difference induced by asymmetric THz radiation coupling, we demonstrate an enhancement in room temperature responsivity from 0.8 V W⁻¹–2.1 V W⁻¹ in self-powered states. The built-in electric field in the NFT/graphene heterojunction further optimizes self-powered performance, achieving a peak responsivity of ~1.4 kV W⁻¹ around 225 K, with a noise equivalent power (NEP) of <20 pW Hz^{-1/2} and a response time of ~0.9 μ s. These results pave the way for the engineering of photodetection mechanisms that offer superior sensitivity and speed, thus opening new avenues for the practical exploration of 2D antiferromagnetic materials and the microscopic correlation mechanisms essential for targeted applications.

Results

Localized behaviour of carriers in the NbFeTe₂

A series of characterization results including Raman, X-ray Diffraction (XRD), Energy Dispersive Spectroscopy (EDS), High-angle annular dark-field (HAADF) imaging are presented in Supplementary Note 1 to confirm the high crystalline quality of NFT for subsequent experiments. In Fig. 2a, we plot the surface band structure along the X- Γ -X direction, probed by ARPES using photon energy $h\nu = 21.2$ eV. The corresponding curvature and energy distribution curve (EDC) are shown in Fig. 2b, c, respectively. Two flatter energy bands, which are located 0.5 eV (α) and 1.5 eV (β) below the Fermi energy level are

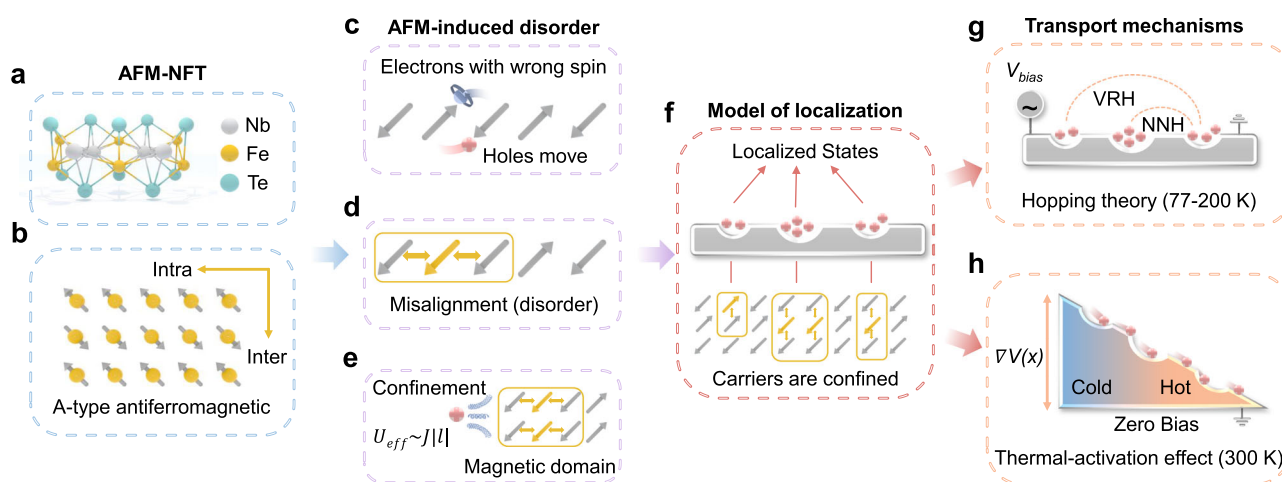


Fig. 1 | Schematic diagram of the antiferromagnetism-induced disorder and pertinent localized transport. **a** The atomic arrangement of NbFeTe₂ (NFT). **b** The magnetic moment distribution within the NFT. **c** Due to the differing spin directions of electrons between the spin lattices of neighboring antiferromagnetic (AFM) phases, the phenomenon of magnetic moment flipping is more likely to occur during carrier transport. **d** This leads to the local formation of magnetic domains caused by magnetic moment disorder, **e** which in turn localizes carrier

transport. Here, the energy expended U_{eff} is proportional to the motion trajectory /length l . **f** Schematic representation of the physical model for carrier localization due to magnetic domains. Modeling of two transport mechanisms for generating photocarriers from localized states: **g** radiative-induced conductance change and **(h)** the self-powered photocurrent associated with Seebeck potential difference ($\nabla V(x)$) induced thermal-activation transport under asymmetrical condition.

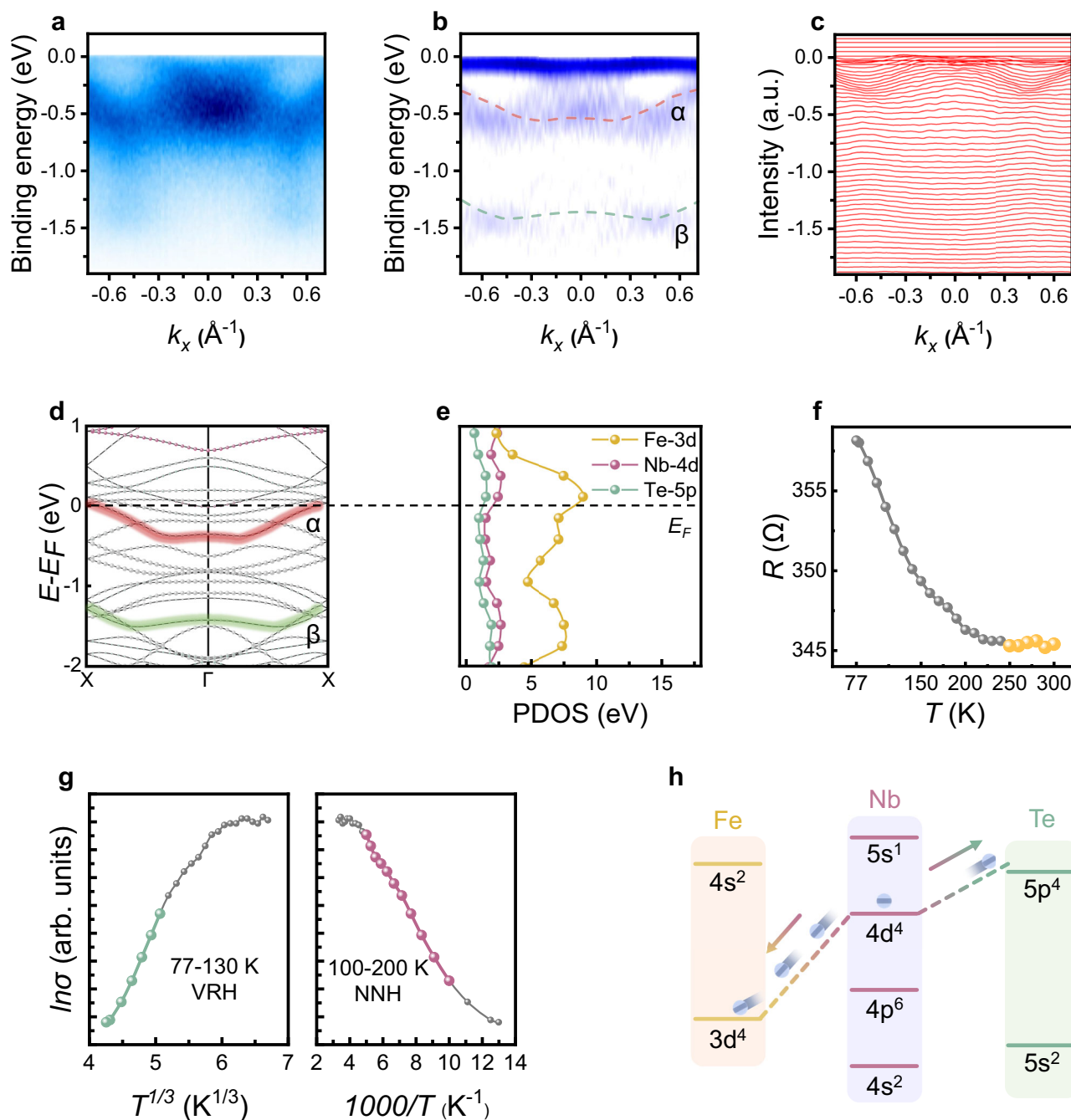


Fig. 2 | Evidence for the existence of localized states in NbFeTe₂ and the hopping transport. The angle resolved photoemission spectroscopy (ARPES) results, including (a) photoemission intensity, (b) curvature, and (c) energy distribution curve (EDC) along the X-Γ-X direction, reveal two distinct and flatter energy bands, labeled as α and β . d The results of the energy band calculations closely coincide with the ARPES data. e The projected density of states (PDOS) results near the Fermi

level. f Resistance hardly changes near 300 K, and the temperature coefficient of resistance (TCR) $\approx -0.04\% \text{ K}^{-1}$ is derived. g The linear relationship between $\ln\sigma$ and $T^{1/3}$, as well as the linear relationship between $\ln\sigma$ and $1/T$, can be considered as evidence for the existence of variable range hopping (VRH) and the nearest neighbor hopping (NNH), respectively. h The calculations of the charge density difference (CDD) reveal the transfer of electrons from Nb to Fe and Te atoms.

clearly identified, and in alignment with the theoretical predictions in Fig. 2d. The procedure for calculating the energy band is detailed in the Method section. In addition, from the Fermi surface in Supplementary Fig. S2c, a large Fermi pocket enclosed by the energy bands and the Fermi surface is observed in the photoemission intensity, representing large carrier effective mass^{25–27}. All these flatter features of energy bands offer clear evidences for the existence of localized states^{28,29}. The projected density of states (PDOS) map in Fig. 2e reveals that the density of states near the Fermi level (indicated by the dashed line) is predominantly contributed by the Fe-3d orbitals. It suggests that the

formation of relatively flat bands α and β is closely associated with the role of Fe atoms.

On the other hand, both ARPES measurement and energy band calculations indicate that the Fermi levels cut through filled bands, endowed with the semimetallic nature. However, the increased resistance with decreasing temperature shown in Fig. 2f contradicts typical metallic characteristics observed in graphene or other semimetals^{30,31}. Notably, the resistance of NFT nearly stabilizes around 300 K, resembling the behavior of an insulator in a disordered system, as described by the Mooij criterion³². Furthermore, cryogenic carrier transport

experiments clearly indicate the variable range hopping (VRH) and the nearest neighbor hopping (NNH) following the Mott's hopping theory as shown in Fig. 2g. This provides additional evidence of magnetic-domain disorder induced localization^{33,34}. Indeed, while most cases of localization in disordered systems result from impurities or defects, such factors were not detected in the scanning transmission electron microscopy (STEM) images or other characterization results (see Supplementary Note 1).

To better understand the mechanism of localization in NFT, the charge density difference (CDD) and the electron transfer process in respect to the Fermi energy as illustrated in Supplementary Fig. 2d are calculated following the density-functional-theory (DFT) calculation. The calculations in Supplementary Table 1 provide direct evidence that the reconstruction of NFT is the most stable in form of the intra-layer ferromagnetic and inter-layer antiferromagnetic magnetic moment arrangement. Additionally, it indicates that the charges are primarily transferred to Fe atoms that contribute most to the magnetic properties, as depicted in Fig. 2h and Supplementary Note 2.

Following the above results, the pictures of carrier transport between spin lattices can be established, as depicted in Fig. 1c–e. When the electrons transition between spin lattices of neighboring antiferromagnetic phases, their spins in opposite directions may alter the orientation of magnetic moments at the initial position, leading to the formation of magnetic domains from locally disordered arrangements of magnetic moments³⁵.

At this juncture, the energy expended U_{eff} during the movement of the hole is directly proportional to the length of its trajectory l . In brief, this localization in NFT caused by the disorder of the magnetic moments, disrupts the periodic arrangement of magnetic moments, causing the Bloch function of electrons to decay exponentially in space, which inherently poses a significant obstacle to carrier transport (Fig. 1f). Thus, by stark contrast with perforated disorder by destroying material with impurities or doping, it adds a modifiable parameter for endowing the electronic hopping with functionalities under external stimuli.

Interplay between hopping and bolometric photocurrent response in symmetric bow-tie detectors

To unveil the effect of the hopping-transport mechanism on THz detection, we integrate the highly symmetric bow-tie antenna structure as shown in Fig. 3a, which increases the coupling strength of THz radiation to provide a direct gateway to manipulate the hopping transport of charges in the channel region, and minimizes the structural imperfection effect as well such as the inhomogeneity of the field strength or locally built-in potential as much as possible.

The temperature coefficient of resistance (TCR) in Fig. 2f is governed by the formula $TCR = (dR/dT)/R_0$, which could reach about $-0.04\% K^{-1}$, and this value is typically smaller than both the metallic and semiconducting bolometers³⁶. It is noteworthy that the NFT possesses a negligible bandgap, whereas the existence of localized states derived either from magnetic interaction or disorder, allowing for the dominated semiconductor-like TCR without physical etching or chemical treatment externally³⁶. The NNH and VRH at different temperature ranges, along with the semi-metallic background conductance, are beneficial for intraband absorption of low-energy photons and the nonequilibrium relaxation among trapped and free carriers.

Here, we explore the feasibility of manipulating the motion of charges under strike by THz electric field and identify the role of hopping transport in antiferromagnetic semimetal for the subsequent detection process. Notably, as delineated in Fig. 3b, the THz radiation thermalizes the electron system, depositing the energy of thermal activation at low bath temperatures for overcoming potential barriers, as a result, the NNH and the resistance reduction can take place.

We initially identify the optimal response at the frequency near 0.11 THz within the 0.08–0.12 THz range as shown in Fig. 3c, and the

spectrum response as well as the optimal frequency-point stay unchanged at different temperatures except the fluctuation in magnitude. By decreasing the temperature, the photocurrent grows up evidently when the NFT turns into the hopping-transport regime at temperatures lower than 200 K, in well-accordance with the trend of resistance change as shown in Fig. 2f. This anomaly is attributable to the improved mobility of the freely-motion carrier at lower temperatures and coupled hopping between thermalized and trapped carriers. In the meantime, the photocurrent grows up linearly under different biases in Fig. 3d, conforming well with the bolometric mechanism of our device^{37,38}.

To show the radiation-heating induced change of transport conductance, Fig. 3e provides direct evidence of the resistance reduction ΔR measured at different temperatures under the same THz radiation. Benefiting from the participation of hopping transport, the ΔR increases by nearly three times even though NFT is semimetal and hosts a large static background conductance. Figure 3f depicts how the photocurrent changes under the On-Off Keying (OOK) of THz light with the modulation frequency range of 1–30 kHz, providing direct evidence for the fast-switching properties of the bolometric detector. The photocurrent (I_{ph}/I_0) is normalized at each temperature to underscore the exact location of the 3 dB bandwidth as indicated in the inset, representing an order of magnitude faster than traditional bolometric ones³⁹.

The photocurrent in the main panel of Fig. 3f at different OOK modulations is growing up at lower temperatures, while the corresponding normalized-photocurrent curves in the inset are practically overlapped, substantiating the 3 dB bandwidth >10 kHz and independent of temperature change. In this regard, the speed of our bolometric device is rivalled with other ones such as phase-change⁴⁰, or disorder-enabled bolometers⁴¹. A possible explanation of the temperature-independent speed is that the NFT is dominated by the portion of transport conductance contributed from freely moving-type electrons due to its gapless nature.

The waveform plots in Fig. 3g further validate the stability of the device when operating at various temperatures. Due to the suppression of thermal-agitation noise and phonon-scattering at lower temperatures, the response is becoming smoother. Furthermore, the temperature dependent responsivity at different bias voltages in Fig. 3h also verifies that hopping transport (<200 K) contributes significantly to the improvement of responsivity, in coincidence with the resistance-temperature behaviour. Nonetheless, as depicted in Supplementary Fig. S4a, when the temperature is below 200 K, the responsivity exhibits a linear relationship with $\ln T$, resembling the hopping transport after the THz illumination. Following the above trend, the VRH would predominate in NFT at temperatures below 77 K in the absence of THz photon excitation. Even though an additional hopping mechanism may result from magnetic interaction such as spin-glass state in NFT at lower temperatures, it can be speculated that the responsivity R_v of the detector can be increased by nearly an order of magnitude ($22 V W^{-1}$) compared with room temperature ($2.5 V W^{-1}$) at low bias voltages (Fig. 3i).

Here, the responsivity is conservatively given by taking into account the diffraction-limit area $S = (\text{when } S \gg S_a, \text{ and } S_a \text{ represents the active area of our device})$ following the relation: $R_v = (I_{ph} \times R)/(P \times S)$. Therefore, the Anderson localization of NFT with Mooij criterion, in along with the interplay between localized states and thermal-activation ones under THz illumination, constitute essential factors of superior bolometric performance in terms of sensitivity and response time.

“Reordered” transport in asymmetric split-ring detectors induced by thermal-activation at room temperature

While the hopping model described above shows great potential for THz detection at low temperatures, carriers are unfortunately still

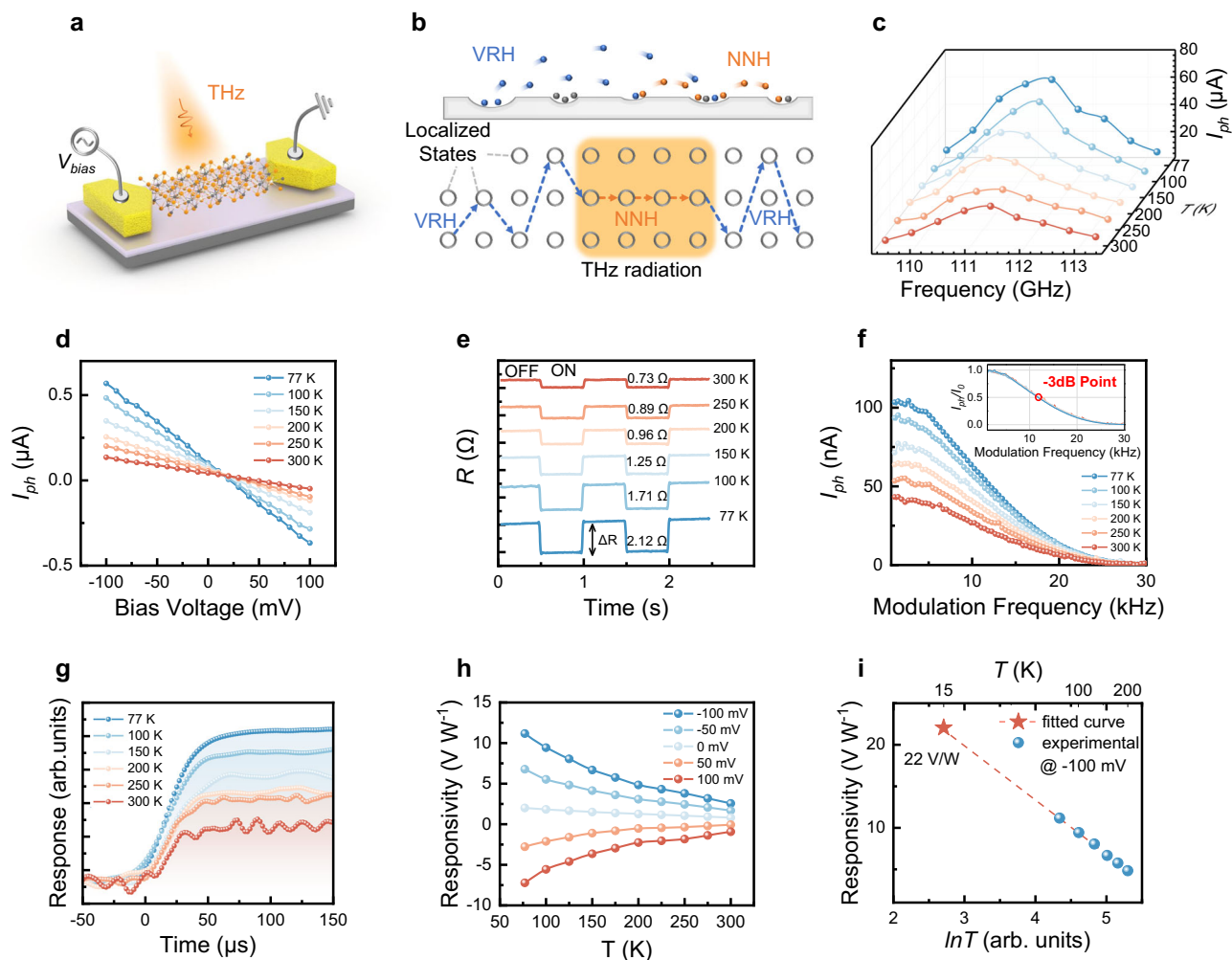


Fig. 3 | Evidence for the presence of hopping and bolometric effects. (symmetric bow-tie devices) **a** Conceptual view of the THz detector integrated with a bow-tie antenna based on NFT. **b** The physical models of carriers hopping which could switch between variable range hopping (VRH) and the nearest neighbor hopping (NNH) under THz radiation. **c** The spectrum response of bolometric device as assisted by the butterfly antenna. **d** The linear voltage-dependence of bolometric response due to the radiation-heating induced conductance change.

e The derived resistance change at different temperatures following the on/off modulated THz radiation at 0.11 THz. **f** The extracted response at different temperatures with 3 dB electrical bandwidth is shown in the inset. **g** The pulsed response of photocurrent at different temperatures exhibits an improved signal-to-noise ratio taken at hopping-transport regime. **h** The responsivity versus temperature at different bias voltage and validation of THz-field induced thermal activation transport in (i).

trapped in localized states around 300 K as shown in Fig. 1f. This limitation significantly hinders the performance of room-temperature THz detection in the NFT bolometer. Here, we propose a strategy to enhance the performance of room-temperature THz detection by selectively manipulating the motion of nonequilibrium carriers. Accordingly, a resonant split-ring antenna with asymmetric capacitive coupling in Fig. 4a, is optimized in terms of electrical connection utilizing the finite difference time domain (FDTD) method, producing non-uniform distribution of localized THz field across the channel. We optimize the size, angle, channel length, and other parameters of split-ring antenna to achieve a peak coupling strength (E/E_0) of -150 which is close to the bow-tie antenna, as illustrated in Supplementary Note 3. More clearly, Fig. 4b reveals that the structure can capture the electromagnetic waves in the channel, improving the light absorption and thermal-activation transport in NFT. Strong localized THz-field emerges around the edges of the two contacts manifesting an obvious difference in strength by five times (inset). On the other hand, the atomic force microscope images in Supplementary Fig. S1h corroborate the homogeneity of the material, indicating that the extrinsic imperfections can be ignored. Due to the asymmetrical coupling, the

thermal-activated carriers can be reordered as presented in Fig. 1h, so that the photocurrent can be generated in a self-powered fashion. As a consequence, the voltage variation $\Delta V(x)$ traverses across the channel phenomenologically following the scheme of $\Delta V(x) = -S(x) \cdot \nabla T(x)$, as shown in Fig. 4c. Besides, it can be grown up and switched into bolometric photocurrent under a bias voltage. Thus, the Anderson localization in NFT with resistivity near Mooij limit holds appealing features in absorbing and detecting high-frequency signals. The photocurrent exhibits good linear-dependent behaviour when sweeping the input power P_{in} from 0 to 35 μW (Supplementary Fig. S4b), holding the dynamic range over 20 dB. In the meantime, the device also exhibits superior polarization selectivity as described in Supplementary Fig. S4c. At different frequency bands, the variation of photocurrent can be qualitatively explained as the selective excitation of electromagnetic coupling strength in sub-wavelength structure as shown in Fig. 4d^{42,43}, apparently different from highly magnetic-field dependent sub-terahertz magnons in antiferromagnetic insulators^{38,39}. While the direction of the photocurrent is independent of photon-frequency, and the pulsed response in Fig. 4e indicates a better signal-to-noise ratio and a stable duty cycle compared with that in Fig. 3g.

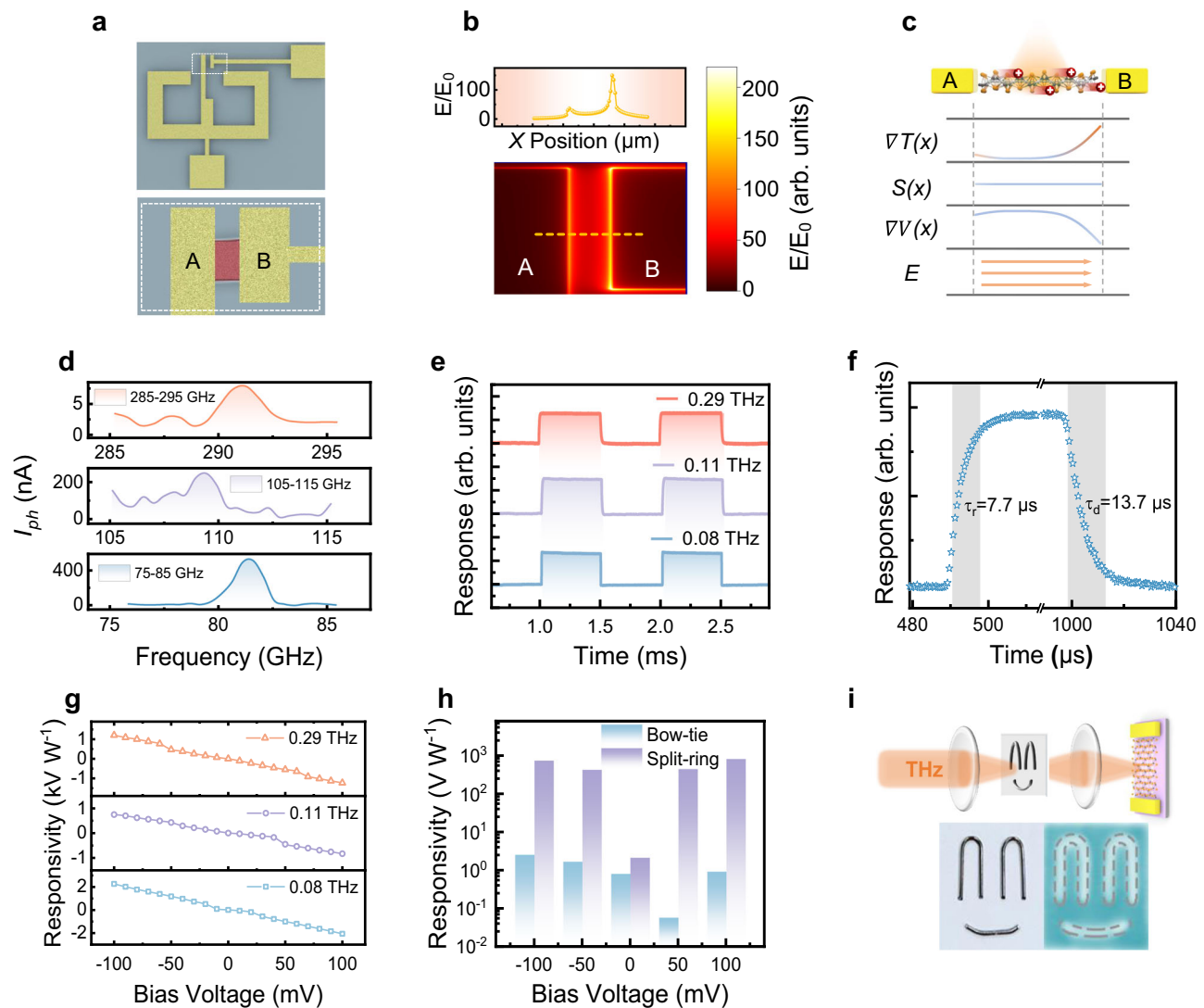


Fig. 4 | Optical response of asymmetric structure NbFeTe₂-based photo-detector at room temperature. (asymmetric split-ring devices) **a** The designed sub-wavelength structure of reordered device, and the channel part is outlined by a white dashed line in along with **(b)** the simulated THz-field profile. The inset depicts the coupling strength distribution at the position of the yellow dashed line. **c** The non-uniform distribution of the localized THz field in the channel generates a potential difference, supplying carriers with the necessary energy to escape from

their localized states. **d** The photocurrent across various frequency bands. **e** Optical response waveforms at different frequencies captured by an oscilloscope. **f** The zero-bias waveform demonstrates a response time of 7.7 μ s and a recovery time of 13.7 μ s. **g** The bias voltage dependent responsivity, showing linear growth at different frequencies. **h** The comparison of responsivity between symmetric bow-tie devices and asymmetric split-ring devices. **i** Scanned THz imaging results clearly reveal the profile of metallic fingers at 0.29 THz.

In the meantime, the response time, defined as the time required for photocurrent rising from 10% – 90% or recovering from 90% to 10% within a single period of radiation, is readable from Fig. 4f, showing a rise time of 7.7 μ s and a fall time of 13.7 μ s, which is obviously faster than that of a typical bolometric device. Under the self-powered zero bias operation, the responsivity of the device is 9 V W^{-1} at 0.08 THz, 2 V W^{-1} at 0.11 THz, and 0.8 V W^{-1} at 0.29 THz (Fig. 4g), respectively. Moreover, when a small bias voltage (-100 mV) is traversing across the channel, the thermal-activated hot carriers are accelerated by the external electric field, leading to prominent linear growth of the responsivity (1.2 kV W^{-1} at 0.29 THz) of the device, in well-accordance with the result of Fig. 3. When comparing room-temperature THz detection performance (Fig. 4h), the reordered carriers demonstrate significantly improved transport ability compared to the disordered regime, resulting in a higher THz responsivity. This verifies the feasibility of the scheme for reordering carrier transport by the Seebeck potential. These extraordinary phenomena prompt our attestation to

the steady status of the device under a bias voltage. As shown in Supplementary Fig. S4d, the time-resolved photocurrent response with different bias voltages is recorded through high-speed oscilloscope, from which it is unambiguously that all the waveforms are well-preserved except the growing up in amplitude at different voltages. Besides, there is no significant decay of the optical response recorded by the source meter after 1 month exposure to the ambient environment in Supplementary Fig. S4e, allowing for the high-resolution imaging at 0.29 THz in Fig. 4i.

Heterojunction detectors for performance enhancement in the self-powered state

Unlike the antiferromagnetic insulator or other bulk forms, the compatibility with other materials as well as localization behaviour, opens up avenues for exploring intriguing photodetection routes. Next, a van der Waals integration of NFT and graphene is envisioned to be an alternative strategy to build up a highly-efficient THz light harvester,

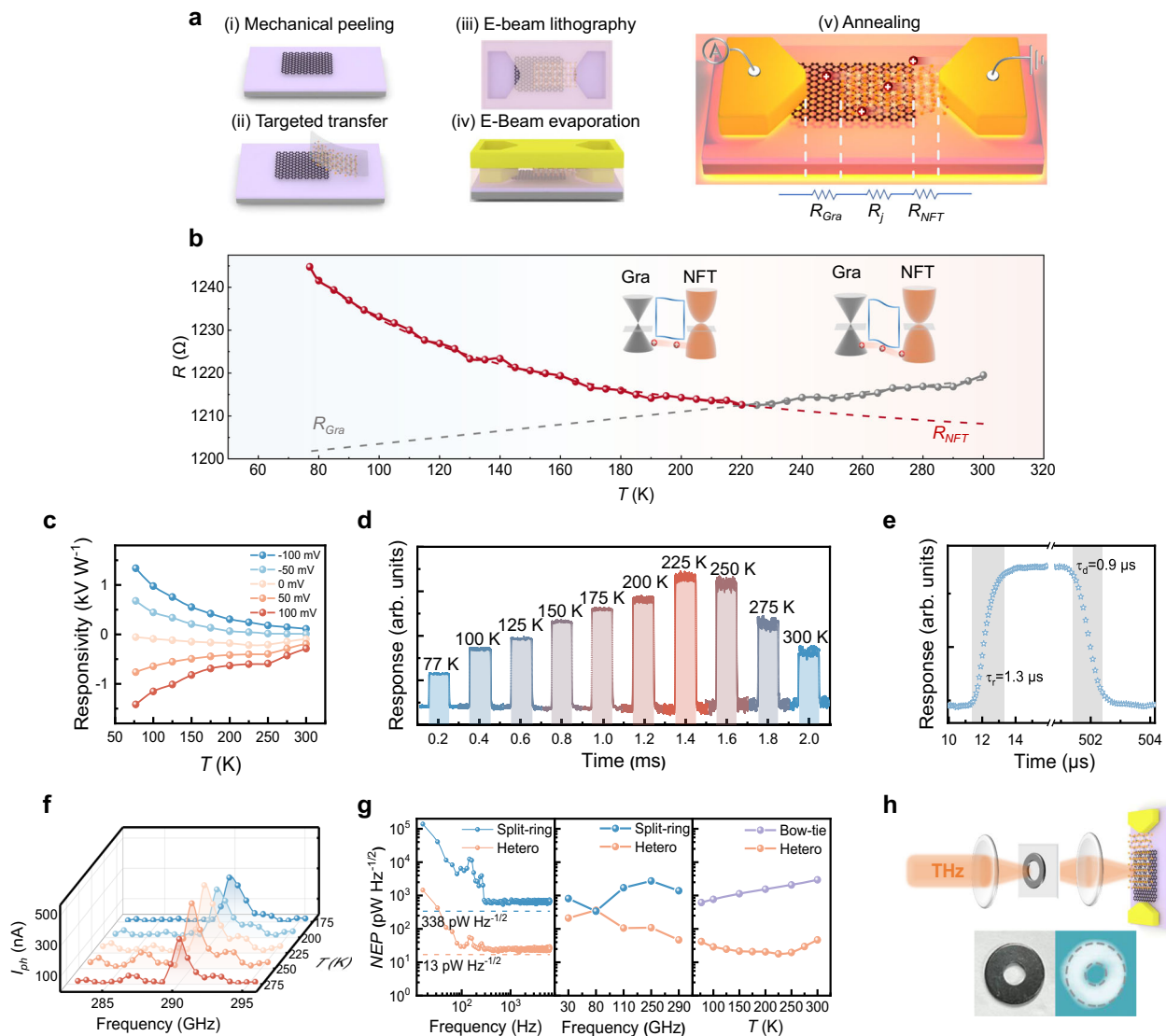


Fig. 5 | Photoresponse of the NFT/graphene heterojunction device. a Process flow for preparing a heterojunction device. The overall resistance is composed of three parts: graphene (R_{Gra}), junction (R_j) and NFT (R_{NFT}). **b** The total resistance is dominated by the graphene part, interfacial junction-resistance and NFT part by decreasing temperatures, and reaches its minimum at 220 K when the interfacial barrier is reduced for thermal-activation transport. **c** The THz photoresponse of the heterojunction measured at different temperatures, and the corresponding pulsed

response is shown in **(d)**. **e** Response speed in self-powered mode of the heterojunction device. **f** The temperature dependent responsivity exhibits hopping-strengthened behaviour under bias. **g** The noise equivalent power (NEP) of heterojunction can be as low as $20 \text{ pW Hz}^{-1/2}$, competitive with other types of devices reported in this work. **h** Imaging results validate the excellent signal-to-noise ratio of the heterojunction.

facilitating the thermal-activation transport of weak-localization states. The incorporation of graphene optimizes the quality of the interfacial ohmic contacts⁴⁴, and not only provides the heterointerface aiding the separation of thermal-activated carriers, but also promotes the responsivity without jeopardizing broadband ability. Notably, to prevent carrier localization interruptions induced by Seebeck potential changes, we employ the same bow-tie antenna mentioned above to compare the performance between NFT bolometer and NFT/graphene heterojunctions.

We conduct a 180°C , 2 h annealing treatment on the heterojunction device in Ar environment before encapsulating it in the dewar to achieve an excellent heterointerface. The process-flow diagram of the hetero-junction device is depicted in Fig. 5a (see also details in the Methods section), and the linear current-voltage character of the hetero-junction with a resistance of 1220Ω is survived as shown in Supplementary Fig. S5a, indicating that the two materials form a high-quality interfacial contact. Here, the device hosts distinctive

temperature-dependent “phase-transition” behaviour similar to the previously mentioned device based on phase-transition materials⁴⁵.

It can be distinguished from Fig. 5b that the resistance R_{ds} is dominated by the graphene part at temperatures above 225 K, below which the junction resistance R_j and hopping-transport resistance R_{NFT} dominates. Meanwhile, due to the difference in Fermi-levels, as well as the different photon absorption from segregated parts of materials in the junction area, thermal-activation nonequilibrium carriers are generated and accelerated by the build-in field in terms of intra-band transport as shown in the inset of Fig. 5b. The spectrum response of photocurrent from 0.283 – 0.297 THz is shown in Fig. 5c and is compared with the asymmetric bow-tie device in Supplementary Fig. S6. A significant growth of photoresponse resembles the “phase-transition” which is identified at 225 K when the interface transport dominates the photocurrent. The self-powered photoresponse possesses advantages with speed an order of magnitude faster than both asymmetric structure and bolometric ones (Fig. 5e) and the

responsivity reaches up to 220 V W^{-1} near 225 K at 0.29 THz. Detailed comparisons of the performance of the three devices described above are provided in Supplementary Notes 5.

When the bias-voltage is traversing across the channel, the temperature dependent photo-response exhibits hopping-strengthen behaviour with responsivity $>1.4 \text{ kV W}^{-1}$ in Fig. 5f, while a stable linear relationship between I_{ph} and bias-voltage persists (Supplementary Fig. S5b). The noise components which are composed of $1/f$ noise generated by the presence of surface defects, thermal noise (v_t) due to carrier perturbation and shot noise (v_s) resulted from carrier crossing the potential barrier in the system, are initially extracted by measuring the noise voltage spectral density (v_n). Since the $1/f$ noise only dominates at lower modulation frequencies ($<1 \text{ kHz}$), and the device in this work can operate stably at modulation frequencies above 5 kHz, at which point the $1/f$ noise can be ignored. Subsequently, the noise equivalent power (NEP) for asymmetric structure and heterojunction devices are determined as $540 \text{ pW Hz}^{-1/2}$ and $20 \text{ pW Hz}^{-1/2}$ in Fig. 5g, respectively. The NEP obtained through equation $NEP = [(v_t^2 + v_s^2)^{1/2}] / R_v = [4k_B T r + 2q I_d r^2]^{1/2} / R_v$ is also informative. Correspondingly, the calculated results ($338 \text{ pW Hz}^{-1/2}$ and $13 \text{ pW Hz}^{-1/2}$) are comparable to the experimental results. The predominantly low NEP further substantiates the role of heterogeneous architecture in suppressing defects diffusion and carrier recombination, and among other factors, creating a conducive environment for carrier hopping. To validate the benefits in improving the signal-to-noise ratio (SNR), Fig. 5h displays the scanned transmission imaging of a metallic ring placed at the focal plane, and the signal is recorded in photocurrent configuration while keeping zero bias-voltage for the hetero-junction devices. It can be seen that the hollow shape of the metallic ring is clearly resolved with sharp edge contrast, and noise in the opaque region is clearly suppressed with $SNR > 1000$. Detailed performance specifications of common THz detectors are compared in Supplementary Table 2 and Fig. S11. Our devices have considerable benefits over THz detectors based on the vast majority of 2D and conventional semiconductor materials, and they are prospective to achieve further optimisation through improved circuit integration and arrayed designs.

Discussion

This study emphasizes the localization characteristics in 2D anti-ferromagnetic materials, revealing the intrinsic properties of charge excitation carriers hopping, which can be effectively utilized in cryogenic THz detection, extending beyond the spin degree of freedom. We specifically present the flat band characteristics linked to localization in the antiferromagnetic semimetal NFT, supported by theoretical calculations and ARPES findings. In this system, localization, driven by the interaction between antiferromagnetic moments and electron spins, allows carriers to hop between localized states via NNH or VRH⁴⁴ mechanisms within the 77–200 K temperature range, resulting in a nonlinear increase in THz responsivity as the temperature decreases. At room temperature, the confinement of carriers within localized states can be mitigated by introducing a Seebeck potential difference through an asymmetric structure, leading to nearly three orders of magnitude increase in device responsivity under a 100 mV bias. Additionally, the built-in electric field of the NFT/graphene heterojunction is employed to enhance self-powered operation, achieving a peak responsivity of 220 V W^{-1} around 225 K, with a NEP of $<20 \text{ pW Hz}^{-1/2}$ and a response time of $\sim 0.9 \mu\text{s}$. These findings offer a direct pathway for addressing targeted applications in the field of THz science and technology.

Methods

Material growth

As described in Supplementary Fig. S1a, Nb (99.99%), Fe (99.99%), and Te (99.99%) are mixed in a molar ratio of 1:1:2 and sealed in a quartz

tube measuring 16 mm in diameter and 150 mm in length. Additionally, 10 mg of iodine is used as transport agent. Subsequently, the quartz tube, sealed under a vacuum level of 10^{-5} Torr by the oxygen/hydrogen welding torch, is placed in a dual-temperature tube furnace. Afterward, the quartz tube needs to be heated to 850/750 °C for 10 days to ensure high crystalline quality. The NFT single crystals are then retrieved from the quartz tube after cooling to room temperature naturally.

The calculation of energy band

The bulk structure relaxation, band structure, and PDOS are performed by first-principal calculations on the ground of DFT. The exchange-correlation potential is approximated by generalized gradient approximation (GGA). The k-point sampling ($4 \times 4 \times 5$) is used for the Brillouin zone in the reciprocal space, and the k-point mesh is generated by Monkhorst-Pack scheme. The energy cutoff is set as 400 eV, and the convergence criterion of self-consistent calculations is 10^{-4} eV for total energy values. All atomic positions and unit cells are optimized until the atomic forces are $<10^{-2} \text{ eV \AA}^{-1}$.

Device fabrication

The fabrication process of the heterojunction device is illustrated in Fig. 5a. NFT and graphene, as 2D materials, rely on weak vdW forces between layers, allowing for the acquisition of high-quality, thin layers through mechanical exfoliation. Due to the thickness of NFT and graphene, priority is given to transferring graphene first. After mechanically exfoliating graphene onto blue tape (Shanghai Onway Technology Co., Ltd.), it is directly attached to a high-resistance silicon wafer ($>10,000 \Omega\text{-cm}$), a standard method for obtaining thin graphene layers. However, NFT requires targeted transfer using polydimethylsiloxane to form precise heterogeneous contacts with graphene. Following material stacking, electrode patterns are etched via electron beam lithography. Subsequently, Cr/Au in contact with the material is deposited via electron beam vapor deposition. Finally, to minimize the impact of impurities introduced by the above process on the experimental results, the devices are annealed in an argon environment at 180 °C for 2 h to further ensure the cleanliness of the material contact interface.

Photoresponse characterization and performance validation

The Agilent E8257D microwave source, in combination with the VDI multiplier link, generates optical radiation in the frequency ranges of 0.08–0.12 THz (1 mW cm^{-2}) and 0.24–0.3 THz (1 mW cm^{-2}), used for stimulating the optical response of devices. Source meter Agilent 2912 and oscilloscopes can be used to immediately monitor changes in current and voltage when turning on and off THz radiation. The weak THz signals are amplified by a preamplifier SR570 in connected to a lock-in amplifier SR830. In the meantime, the modulated signal controlling the ON/OFF switching of THz radiation is also sent into lock-in amplifier as the external reference signal to effectively suppress background noise, as shown in Supplementary Fig. S9. Since our device is much smaller than the wavelength of incident radiation, the voltage responsivity is then determined by using the relation $R_v = (I_{ph} * R) / (P * S_\lambda)$, where $S_\lambda = \lambda^2 / 4$ is the diffraction-limited area (since the antenna area is $< S_\lambda$) and P^* is the power-flux density.

To test the temperature-dependent behaviour of the NFT-based device, the devices are liquid-cryogenic cooling with a glass window placed at the front of the device. The responsivity is also calculated conservatively without taking into account the loss of THz power delivered across the window. An associated temperature control system is in charge of maintaining the temperature of the chamber within a narrow range of $\pm 0.5 \text{ K}$ to ensure the accuracy of the experiments.

Terahertz imaging system

In Supplementary Fig. S10, the THz imaging system composed of a THz source, off-axis parabolic mirrors, lock-in amplifiers, and electromotive

translation stage is depicted. These components synergistically focus and direct the terahertz radiation onto both the imaging object and the detector. The off-axis parabolic mirrors are key components for effective collimation and focusing of the radiation. A diaphragm is employed to pinpoint the spot position and shield against stray light. The imaging object, measuring 3×3 cm, is segmented into a grid of 100×100 pixels and positioned on the translation stage. In the scanning process, this stage moves incrementally by 0.3 mm to facilitate point-by-point imaging. The detector captures the photocurrent resulting from the THz transmission through the object. This current is then amplified, recorded, and analysed by lock-in amplifiers and backend software, respectively, allowing us to reconstruct the metal object's morphology based on the photocurrent distribution.

Data availability

The data generated in this study are available in the Supplementary Information/Source Data File. Source data are provided with this paper.

References

- Stantchev, R. L., Yu, X., Blu, T. & Pickwell-MacPherson, E. Real-time terahertz imaging with a single-pixel detector. *Nat. Commun.* **11**, 2535 (2020).
- Nagatsuma, T., Ducournau, G. & Renaud, C. C. Advances in terahertz communications accelerated by photonics. *Nat. Photonics* **10**, 371–379 (2016).
- Gu, L. L. et al. A biomimetic eye with a hemispherical perovskite nanowire array retina. *Nature* **581**, 278–282 (2020).
- Kutas, M. et al. Terahertz quantum sensing. *Sci. Adv.* **6**, eaaz8065 (2020).
- Mehdi, I., Siles, J. V., Lee, C. & Schlecht, E. THz diode technology: status, prospects, and applications. *Proc. IEEE* **105**, 990–1007 (2017).
- Sizov, F. & Rogalski, A. THz detectors. *Prog. Quant. Electron.* **34**, 278–347 (2010).
- Long, M. S., Wang, P., Fang, H. H. & Hu, W. D. Progress, challenges, and opportunities for 2D material based photodetectors. *Adv. Funct. Mater.* **29**, 1803807 (2019).
- Fiori, G. et al. Electronics based on two-dimensional materials. *Nat. Nanotechnol.* **9**, 1063–1063 (2014).
- Vicarelli, L. et al. Graphene field-effect transistors as room-temperature terahertz detectors. *Nat. Mater.* **11**, 865–871 (2012).
- Deng, T. et al. Three-dimensional graphene field-effect transistors as high-performance photodetectors. *Nano Lett.* **19**, 1494–1503 (2019).
- Bandurin, D. A. et al. Resonant terahertz detection using graphene plasmons. *Nat. Commun.* **9**, 5392 (2018).
- Wu, X. et al. Antiferromagnetic-ferromagnetic heterostructure-based field-free terahertz emitters. *Adv. Mater.* **34**, e2204373 (2022).
- Cheng, G. H. et al. Emergence of electric-field-tunable interfacial ferromagnetism in 2D antiferromagnet heterostructures. *Nat. Commun.* **13**, 7348 (2022).
- Vaidya, P. et al. Subterahertz spin pumping from an insulating antiferromagnet. *Science* **368**, 160–165 (2020).
- Li, J. et al. Spin current from sub-terahertz-generated antiferromagnetic magnons. *Nature* **578**, 70–74 (2020).
- Hortensius, J. et al. Coherent spin-wave transport in an antiferromagnet. *Nat. Phys.* **17**, 1001–1006 (2021).
- Chen, X. Z. et al. Observation of the antiferromagnetic spin Hall effect. *Nat. Mater.* **20**, 800–804 (2021).
- Zhou, Y. et al. Spin-torque-driven antiferromagnetic resonance. *Sci. Adv.* **10**, eadk7935 (2024).
- Kampfrath, T. et al. Coherent terahertz control of antiferromagnetic spin waves. *Nat. Photonics* **5**, 31–34 (2011).
- Huang, C. et al. Extreme terahertz magnon multiplication induced by resonant magnetic pulse pairs. *Nat. Commun.* **15**, 3214 (2024).
- Yan, H. et al. Electric-field-controlled antiferromagnetic spintronic devices. *Adv. Mater.* **32**, e1905603 (2020).
- Bai, W. et al. Intrinsic negative magnetoresistance in Van Der Waals FeNbTe₂ single crystals. *Adv. Mater.* **31**, 1900246 (2019).
- Yin, L. et al. High-performance memristors based on ultrathin 2D copper chalcogenides. *Adv. Mater.* **34**, e2108313 (2022).
- Guo, Q. et al. Efficient electrical detection of mid-infrared graphene plasmons at room temperature. *Nat. Mater.* **17**, 986–992 (2018).
- Medjanik, K. et al. Direct 3D mapping of the Fermi surface and Fermi velocity. *Nat. Mater.* **16**, 615–621 (2017).
- Kunisada, S. et al. Observation of small Fermi pockets protected by clean CuO₂ sheets of a high-T_c superconductor. *Science* **369**, 833–838 (2020).
- Broyles, C. et al. Revealing a 3D Fermi surface pocket and electron-hole tunneling in UTe₂ with quantum oscillations. *Phys. Rev. Lett.* **131**, 036501 (2023).
- Martinez, J. G. C., Chiu, C. S., Smitham, B. M. & Houck, A. A. Flat-band localization and interaction-induced delocalization of photons. *Sci. Adv.* **9**, eadj7195 (2023).
- He, Y. Y. et al. Flat-band localization in creutz superradiance lattices. *Phys. Rev. Lett.* **126**, 103601 (2021).
- Sumithra, S. et al. Enhancement in thermoelectric figure of merit in nanostructured Bi₂Te₃ with semimetal nano-inclusions. *Adv. Energy Mater.* **1**, 1141–1147 (2011).
- Zhou, J. D. et al. Large-area and high-quality 2D transition metal telluride. *Adv. Mater.* **29**, 1603471 (2017).
- Mooij, J. H. Electrical-conduction in concentrated disordered transition-metal alloys. *Phys. Status Solidi. A* **17**, 521–530 (1973).
- Ying, T. P. et al. Anderson localization of electrons in single crystals: Li_xFe₇Se₈. *Sci. Adv.* **2**, e1501283 (2016).
- Liao, J. et al. Observation of Anderson localization in ultrathin films of three-dimensional topological insulators. *Phys. Rev. Lett.* **114**, 216601 (2015).
- Khomskii, D. *Transition Metal Compounds*. (Cambridge University Press, 2014).
- Sassi, U. et al. Graphene-based mid-infrared room-temperature pyroelectric bolometers with ultrahigh temperature coefficient of resistance. *Nat. Commun.* **8**, 14311 (2017).
- Li, M. Y. et al. Ion-bolometric effect in grain boundaries enabled high photovoltage response for NIR to terahertz photodetection. *Adv. Funct. Mater.* **33**, 2213970 (2023).
- Koepfli, S. M. et al. Metamaterial graphene photodetector with bandwidth exceeding 500 gigahertz. *Science* **380**, 1169–1174 (2023).
- Chiang, S. Y., Li, Y. Y., Shen, T. L., Hofmann, M. & Chen, Y. F. 2D material-enabled nanomechanical bolometer. *Nano Lett.* **20**, 2326–2331 (2020).
- Wu, D. et al. Ultrabroadband photosensitivity from visible to terahertz at room temperature. *Sci. Adv.* **4**, eaao3057 (2018).
- Agarwal, H. et al. Ultra-broadband photoconductivity in twisted graphene heterostructures with large responsivity. *Nat. Photonics* **17**, 1047–1053 (2023).
- Viti, L. et al. Heterostructured hBN-BP-hBN nanodetectors at terahertz frequencies. *Adv. Mater.* **28**, 7390–7396 (2016).
- Asgari, M. et al. Chip-scalable, room-temperature, zero-bias, graphene-based terahertz detectors with nanosecond response time. *ACS Nano* **15**, 17966–17976 (2021).
- Wu, Y. et al. All-transfer electrode interface engineering toward harsh-environment-resistant MoS₂ field-effect transistors. *Adv. Sci.* **35**, 2210735 (2023).
- Li, W. B., Qian, X. F. & Li, J. Phase transitions in 2D materials. *Nat. Rev. Mater.* **6**, 829–846 (2021).

Acknowledgements

L. W. acknowledges funding by the Strategic Priority Research Program of the Chinese Academy of Sciences (No. XDB0580000), the National Key R&D Program of China (No. 2021YFB2800700), National Natural Science Foundation of China (No. 62322515) and Programs of Shanghai Science and Technology Commission (No. 22501100202, No. 24ZR1493100). K. Z. acknowledges funding by National Natural Science Foundation of China (No. T2325025) and Jiangsu Province Key R&D Program (No. BE2021007-3). F. W. acknowledges funding by the Hundred Talents Program of the Chinese Academy of Sciences. W. D. H. acknowledges funding by the Strategic Priority Research Program of the Chinese Academy of Sciences (No. XDB0580000) and the National Key R&D Program of China (No. 2023YFB3611400). Z. D. acknowledges the National Natural Science Foundation of China (No. 62304241), the China Postdoctoral Science Foundation (No. 2023M742553) and the Jiangsu Funding Program for Excellent Postdoctoral Talent. L. B. Z. acknowledges the National Natural Science Foundation of China (No. 62305077) and the China Postdoctoral Science Foundation (Nos. 2023M743652, GZB20230796). The authors acknowledge the support from Analytical Instrumentation Center (#SPST-AIC10112914), Soft Matter Nanofab (#SPST-SMN180827) and Quantum Device Lab, Shanghai Tech University.

Author contributions

D. W., L. Y. and Z. H. contributed equally to this work. L. W., K. Z. and W. H. proposed and conceived this work, D. W., F. W., L. Y. and Z. H. were responsible for experimental design. Z. D., K. Z., M. J. and X. P. performed the majority of the photoelectronic measurements. S. T. and Y. Y. were primarily responsible for materials-related first principles calculations. K. T. and F. D. contributed to the material growth and characterization. L. H. and L. Z. assisted the device simulation. W. L. and X. C. developed the hopping dynamic model with discussions with W. H., D. W. and L. W. wrote the manuscript with comments from all the authors. All authors discussed the results and commented on the manuscript.

Competing interests

The authors declare no competing interests.

Additional information

Supplementary information The online version contains supplementary material available at <https://doi.org/10.1038/s41467-024-55426-0>.

Correspondence and requests for materials should be addressed to Fang Wang, Kai Zhang or Lin Wang.

Peer review information *Nature Communications* thanks Alejandro Kunold and the other, anonymous, reviewer(s) for their contribution to the peer review of this work. A peer review file is available.

Reprints and permissions information is available at <http://www.nature.com/reprints>

Publisher's note Springer Nature remains neutral with regard to jurisdictional claims in published maps and institutional affiliations.

Open Access This article is licensed under a Creative Commons Attribution-NonCommercial-NoDerivatives 4.0 International License, which permits any non-commercial use, sharing, distribution and reproduction in any medium or format, as long as you give appropriate credit to the original author(s) and the source, provide a link to the Creative Commons licence, and indicate if you modified the licensed material. You do not have permission under this licence to share adapted material derived from this article or parts of it. The images or other third party material in this article are included in the article's Creative Commons licence, unless indicated otherwise in a credit line to the material. If material is not included in the article's Creative Commons licence and your intended use is not permitted by statutory regulation or exceeds the permitted use, you will need to obtain permission directly from the copyright holder. To view a copy of this licence, visit <http://creativecommons.org/licenses/by-nc-nd/4.0/>.

© The Author(s) 2024